Supplementary Information for

Polarization Vortices in a Ferromagnetic Metal via Twistronics

Yingzhuo Lun[1,2,#,*], Xinxin Hu[2,3,#], Qi Ren[1,#], Umair Saeed[2,3], Kapil Gupta[2], Bernat Mundet[2], Ivan Pinto-Huguet[2,3], José Santiso[2], Jessica Padilla-Pantoja[2], José Manuel Caicedo Roque[2], Yunpeng Ma[4], Qian Li[4], Gang Tang[1], David Pesquera[2], Xueyun Wang[1], Jiawang Hong[1,5,*], Jordi Arbiol[2,6,*], and Gustau Catalan[2,6,*]

[1]School of Aerospace Engineering, Beijing Institute of Technology, Beijing 10081, China
[2]Catalan Institute of Nanoscience and Nanotechnology - ICN2 (CSIC & BIST), Barcelona, Catalonia 08193, Spain
[3]Autonomous University of Barcelona, Barcelona, Catalonia 08193, Spain
[4]State Key Laboratory of New Ceramic Materials, School of Materials Science and Engineering, Tsinghua University, Beijing 10084, China
[5]Beijing Institute of Technology (Zhuhai), Zhuhai 519088, China
[6]Institució Catalana de Recerca i Estudis Avançats (ICREA), Barcelona 08010, Catalonia

[#]These authors contributed equally to this work.
[*]Corresponding author emails: lunyingzhuo@bit.edu.cn (Y.L.), hongjw@bit.edu.cn (J.H.), arbiol@icrea.cat (J.A.), gustau.catalan@icn2.cat (G.C.)

This PDF file includes:

Supplementary Text I

Supplementary Figures S1 to S17

References

Supplementary Text I: Strain-gradient origin of polar vortices in t-BL SROs

The periodic misalignment of the atoms in the top and bottom layers can generate inhomogeneous interlayer interactions and torsional deformation (shear strain) within the lattice. In principle, the shear strain gradients arisen from inhomogeneous torsion gives rise to flexoelectric fields, which can serve as pseudo-electric fields, modulating polarization and driving the formation of polar vortices. It is nevertheless legitimate to question whether (or how) the flexoelectric effect can still effectively manipulate topological polarization in the presence of electric screening from free charge carriers in a metal. To investigate flexoelectric coupling in metallic SRO bilayers, we employed geometric phase analysis (GPA)[1] to calculate the shear and normal strains (Supplementary Figs. S10 and S11) on the lattice structure observed at STEM-HAADF images (Supplementary Fig. S6). We found that only the shear strains exhibit a periodic distribution that closely follows the moiré pattern and highly correlates with the arrangement of polarization vortices (Fig. 2 in main text). We then computed the derivatives of the shear strain (ε_{xy}) along the *x*-axis and *y*-axis to extract the shear strain gradient components ($\varepsilon_{xy,x}$ and $\varepsilon_{xy,y}$) (Supplementary Fig. S10). The corresponding flexoelectric field[2] can be calculated as

$$\mathbf{E}_{\mathbf{flexo}} = \left(E_x, E_y\right) = f_{xyxy}^{eff}\left(\varepsilon_{xy,y}\hat{\mathbf{E}}_{\mathbf{i}} + \varepsilon_{xy,x}\hat{\mathbf{E}}_{\mathbf{j}}\right) \quad \text{(S1)}$$

where $\mathbf{E}_{\mathbf{flexo}}$ is a total flexoelectric field. E_x and E_y are in-plane components. $\hat{\mathbf{E}}_{\mathbf{i}}$ and $\hat{\mathbf{E}}_{\mathbf{j}}$ are unit vectors in the *x*-direction and *y*-direction, respectively. f_{xyxy}^{eff} is an effective flexoelectric coupling coefficient. According to the above model, the shear strain gradients of $\varepsilon_{xy,x}$ and $\varepsilon_{xy,y}$ can generate pseudo-electric field components in the *y*-direction and *x*-direction, respectively, which in principle can polarize the lattice both vertically and horizontally. To explore the coupling between strain gradient and polarization, we superimposed the strain gradient maps and the measured Ru displacement components (Supplementary Fig. S10). We find that the strain gradients are distributed in a strip network of alternating signs, with the polarization components pointing in the same direction within each strip region, thus evidencing a direct correlation between the polarization and the direction of the strain gradients. The polarization systematically switches towards the opposite direction upon the reversal of the strain gradients.

On this basis, we reconstructed the total flexoelectric field from the shear strain gradients using eq. (S1) with a unit flexoelectric coefficient. The normalized flexoelectric field maps are presented in Main text Figs. 2j-l and Supplementary Fig. S8, superimposed with the toroidal moment (calculated in a similar way to $Q(\delta_{Ru})$). The results show a significant correlation between the flexoelectric fields and measured polarization vortices, providing evidence of a flexoelectric (strain gradient) origin for the polar vortices in metallic twisted bilayers. The above-established electromechanical coupling provides further insights into the origin of the observed twist angle-dependent polarization. We compared the shear strains and corresponding strain gradients within different t-BL SROs, and found that they follow the same twist-dependence as polarization (Supplementary Fig. S12). The larger polarization at small angle originates from the more significant lattice distortion (shear strain) and its localized inhomogeneity (strain gradient).

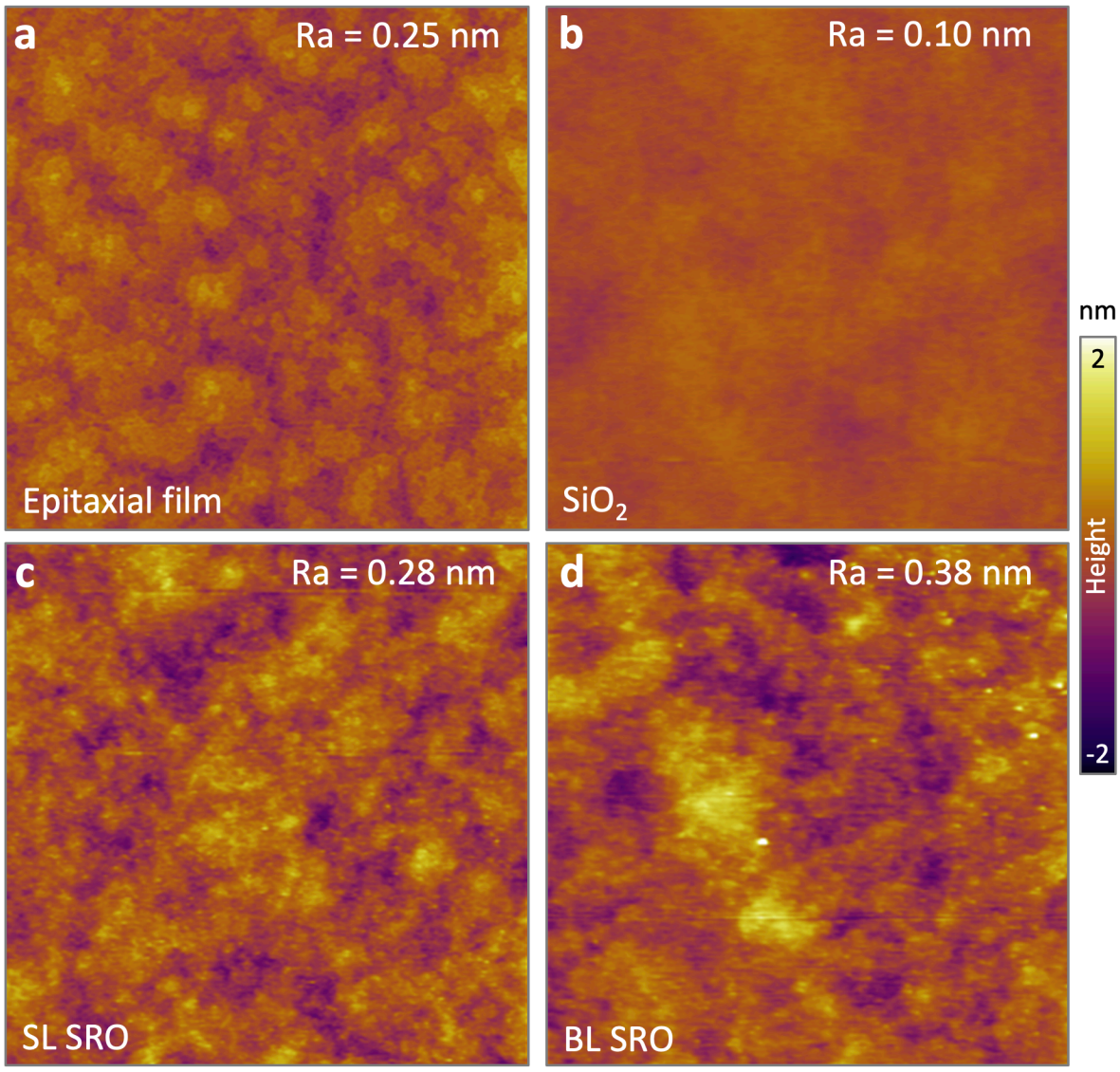

Supplementary Figure S1. High-resolution topographic atomic force microscopy (AFM) images (2x2 μm^2) and corresponding surface roughness (Ra) of **a**, epitaxial film, **b**, oxidized silicon substrate, **c**, transferred single layer SRO, and **d**, twisted bilayer SRO.

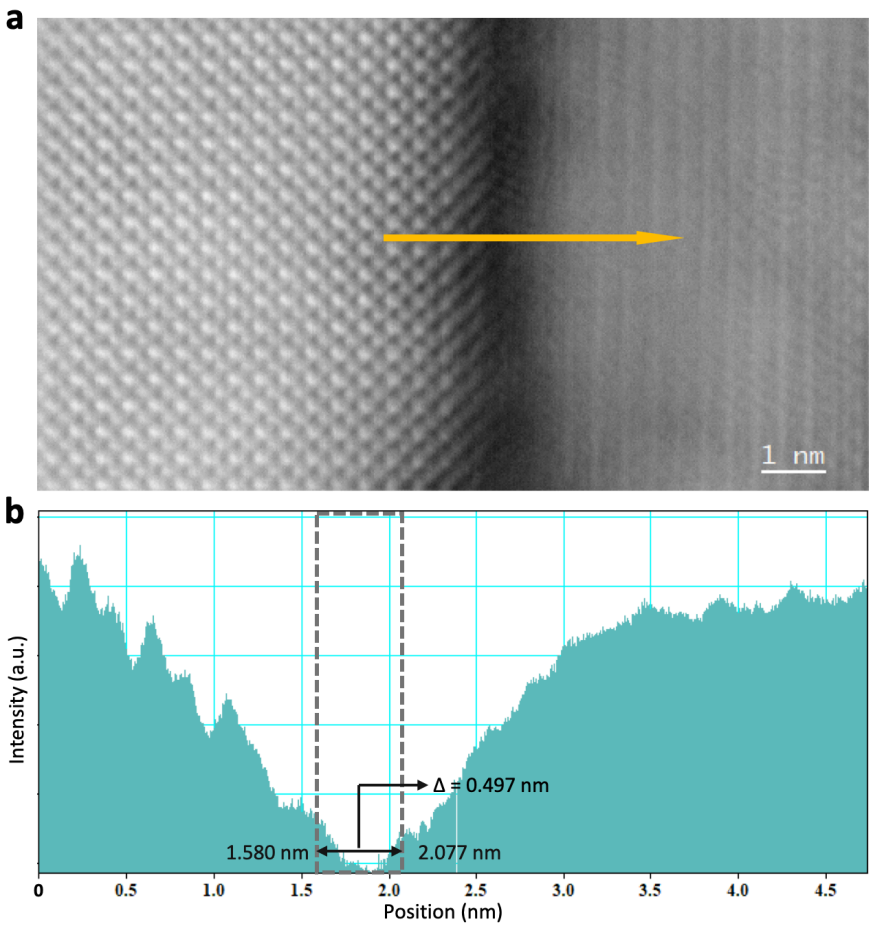

Supplementary Figure S2. **a**, Fourier-filtered STEM-HAADF (cross-section) image of a transferred 4.8° twisted bilayer. **b**, Intensity profile along the highlighted arrow in **a** depicting an interlayer distance of 4.97Å, which is approximately one unit cell in magnitude.

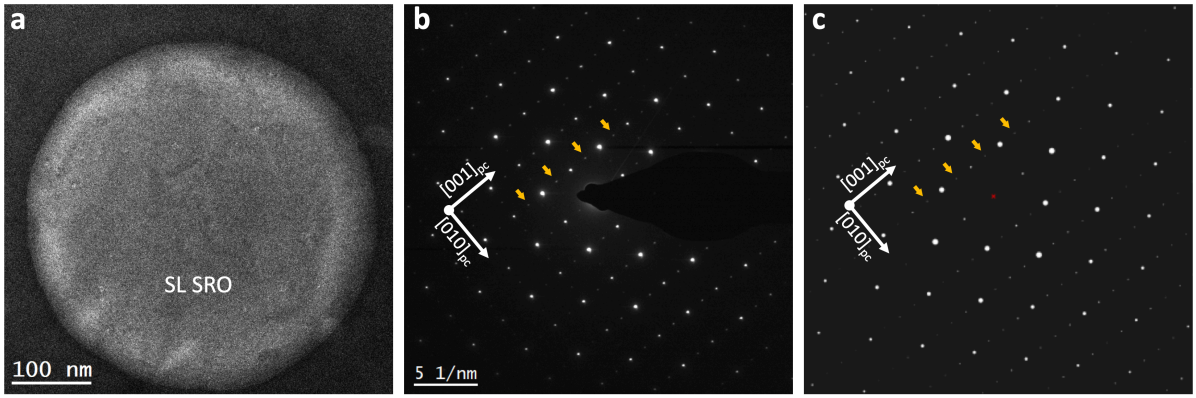

Supplementary Figure S3. a, Low-magnification HRTEM image of a freestanding single-layer SRO membrane. **b**, Corresponding selected area electron diffraction (SAED) image. **c**, Simulated SAED pattern of a $[100]_{pc}$-oriented orthorhombic SRO structure using Recipro software[3]. The yellow arrows indicate the ½ superlattice diffraction spots. The experimental pattern matches well with the simulated one, indicating orthorhombic characteristics of the freestanding SRO membrane.

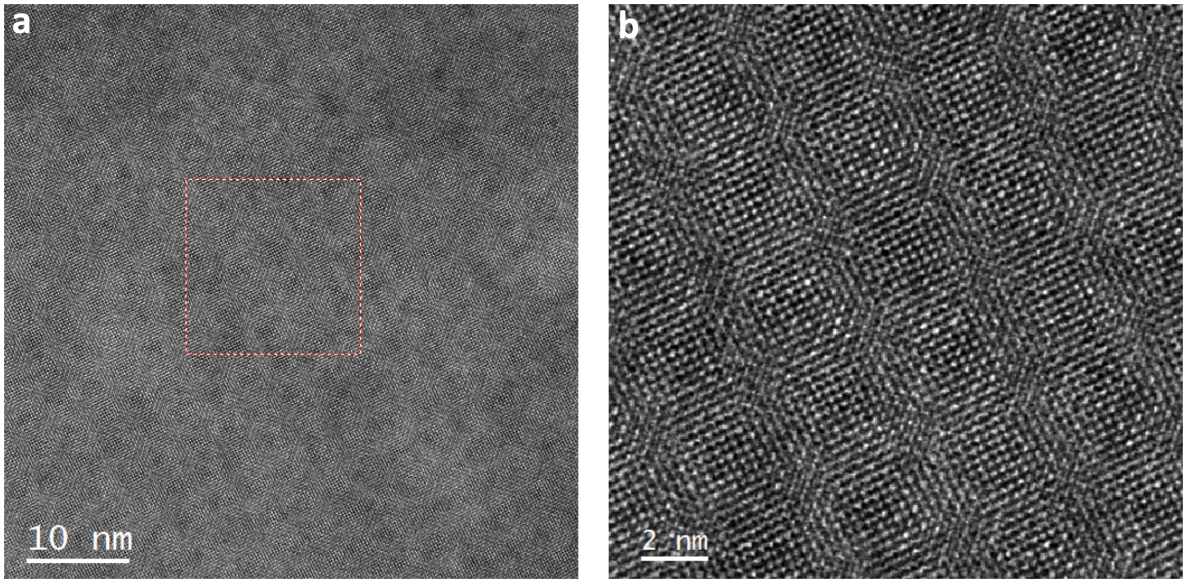

Supplementary Figure S4. a, Low-magnification annular dark-field (ADF) image focusing on the bilayer interface of 4.8° twisted bilayer, revealing a continuous and well-ordered moiré pattern. **b**, Magnified view of the region highlighted in **a**, showing detailed moiré features.

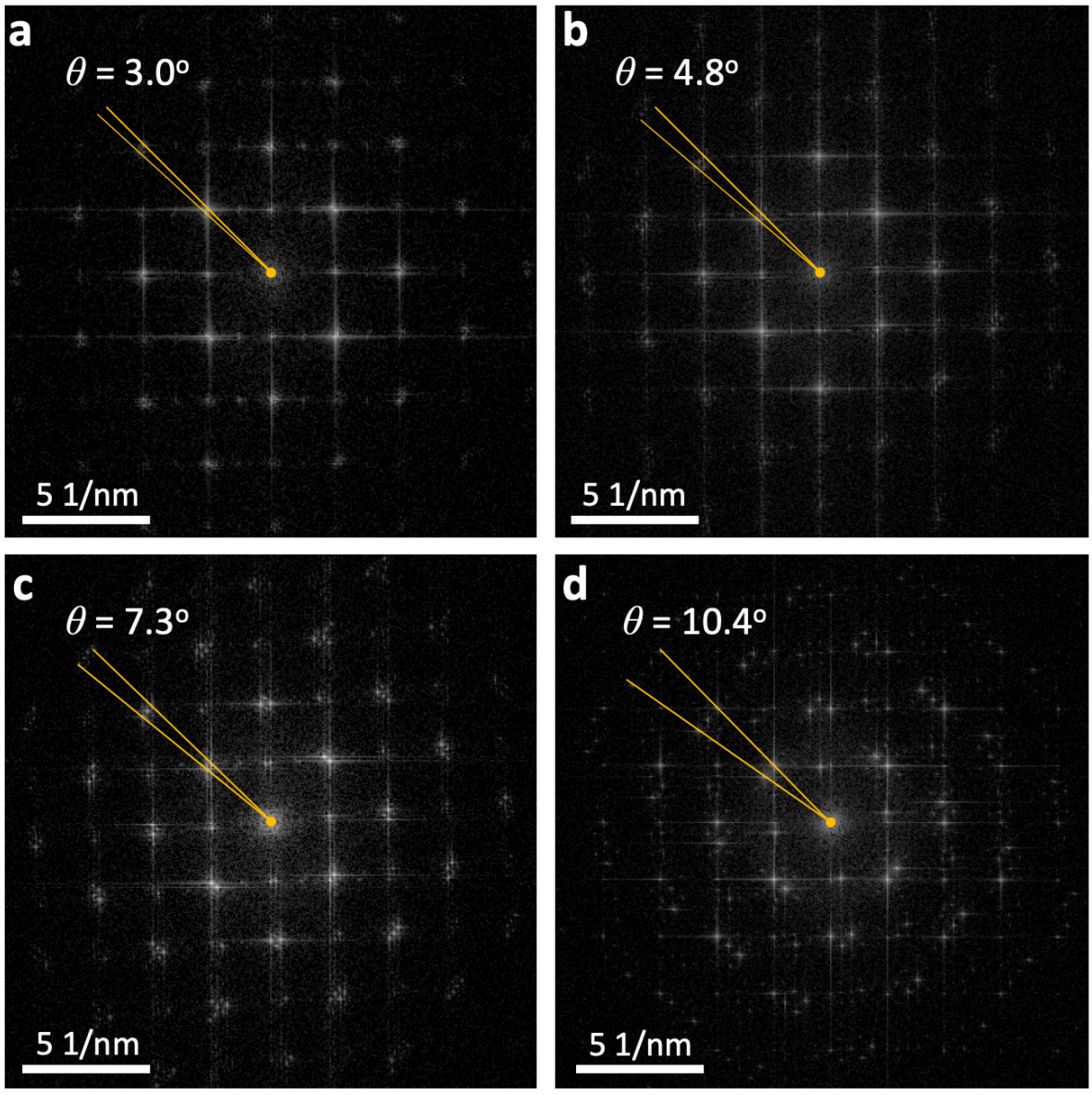

Supplementary Figure. S5. a-d, Fast Fourier transform (FFT) patterns corresponding to the STEM-HAADF images focusing on the bilayer interface in the 3.0°, 4.8°, 7.3°, and 10.4° twisted bilayers, respectively. Each FFT pattern exhibits two distinct sets of diffraction spots arising from the top and bottom lattices. The twist angle is determined based on the relative rotation (indicated by two yellow lines) between the two sets of diffraction spots.

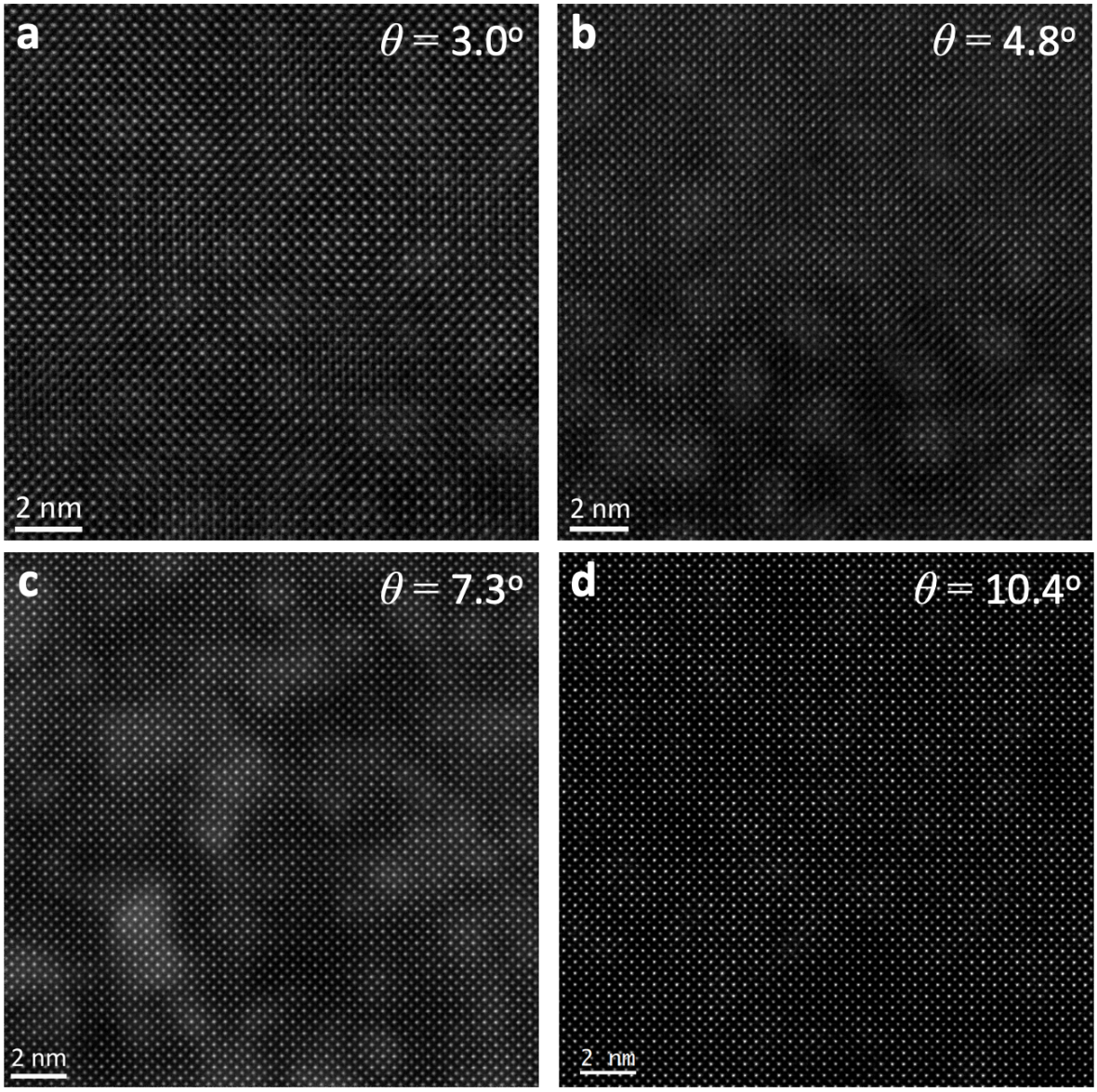

Supplementary Figure. S6. a-d, Planar-view STEM-HAADF images focusing on the upper surface of the top layer in the 3.0°, 4.8°, 7.3°, and 10.4° twisted bilayers, respectively.

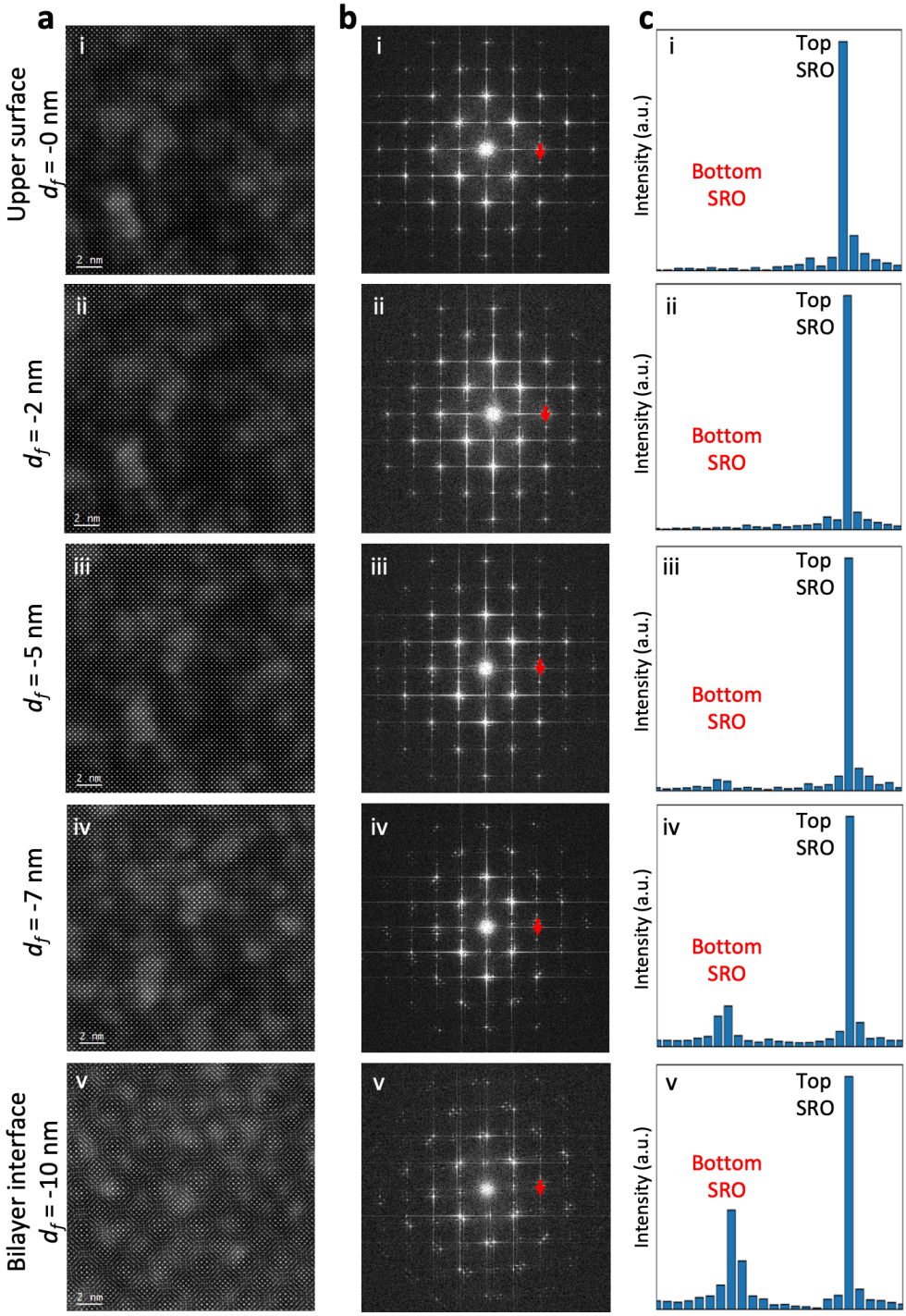

Supplementary Figure S7. a, Planar-view STEM-HAADF images of the 7.3° twisted bilayer obtained at different focus depths (d_f), capturing structural variations from the bilayer interface to the upper surface of the top layer. **b**, Corresponding fast Fourier transform (FFT) patterns extracted from the STEM-HAADF images. **c**, Line profiles taken at the $[2\text{-}20]_o$ diffraction spots (indicated by red arrows) in the FFT patterns, illustrating the evolution of intensity from the bilayer interface to the upper surface. As shown in Fig. c, the intensity of diffraction spot arisen from bottom SRO layer vanishes gradually as shifting the focus away from bilayer interface to upper surface, indicating that the STEM-HAADF image focusing on the upper surface selectively captures the lattice structure of the top layer.

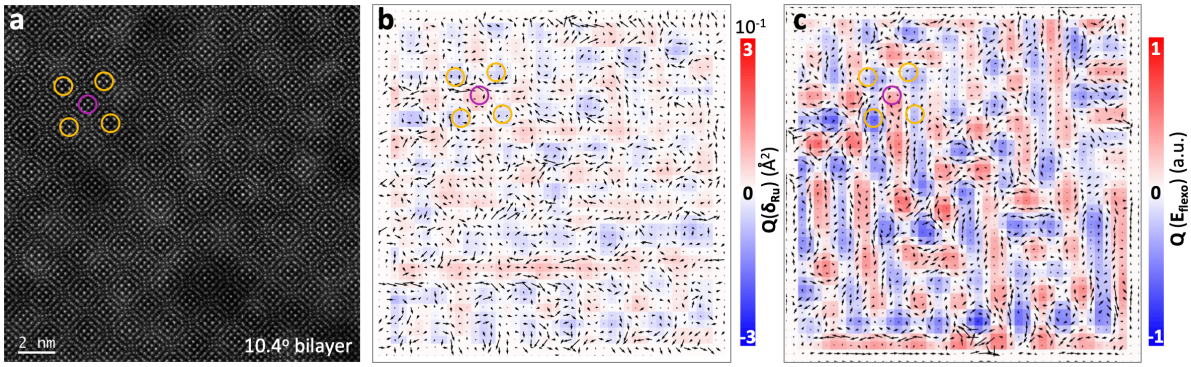

Supplementary Figure. S8. a, Planar-view STEM-HAADF images focusing on the interface in the 10.4° twisted bilayer, showing distinct moiré patterns. **b**, Ru displacement maps of the top layer superimposed with their toroidal moment $Q(\delta_{Ru})$. The Ru displacements are amplified by a factor of 120 for clarity. **c**, Normalized flexoelectric field vector maps induced by shear strain gradients in the top layer, superimposed with their toroidal moment $Q(E_{flexo})$. The yellow and purple circles indicate the AA- and AB-stacked regions, respectively.

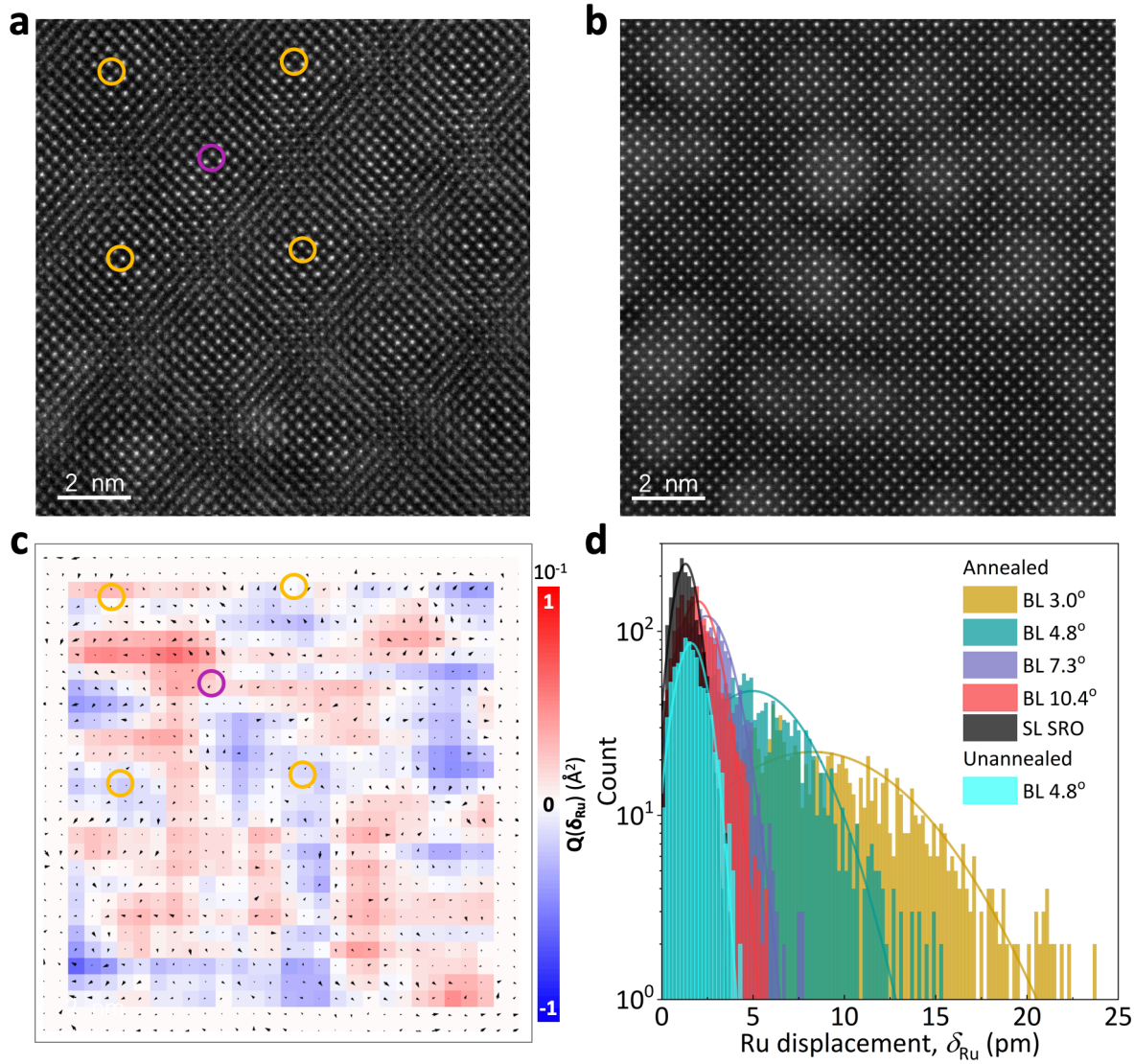

115

116 **Supplementary Figure. S9.** Planar-view STEM-HAADF images of the 4.8° twisted bilayer
117 without annealing, focusing on **a**, the bilayer interface and **b**, the upper surface of the top
118 layer, respectively. **c**, Ru displacement map of the top layer superimposed with the toroidal
119 moment (*Q*). All Ru displacements are amplified by a factor of 50 (same factor used for the
120 annealed 4.8° twisted bilayer). The yellow and purple circles in **a** and **c** indicate the AA- and
121 AB-stackings. **d**, Histograms comparing the magnitude of Ru displacement in annealed and
122 unannealed samples. As shown in **c** and **d**, the Ru displacements in the unannealed samples
123 are both random and minimal (1.6 pm on average), suggesting a nonpolarized state similar to
124 that of SL SRO.

125

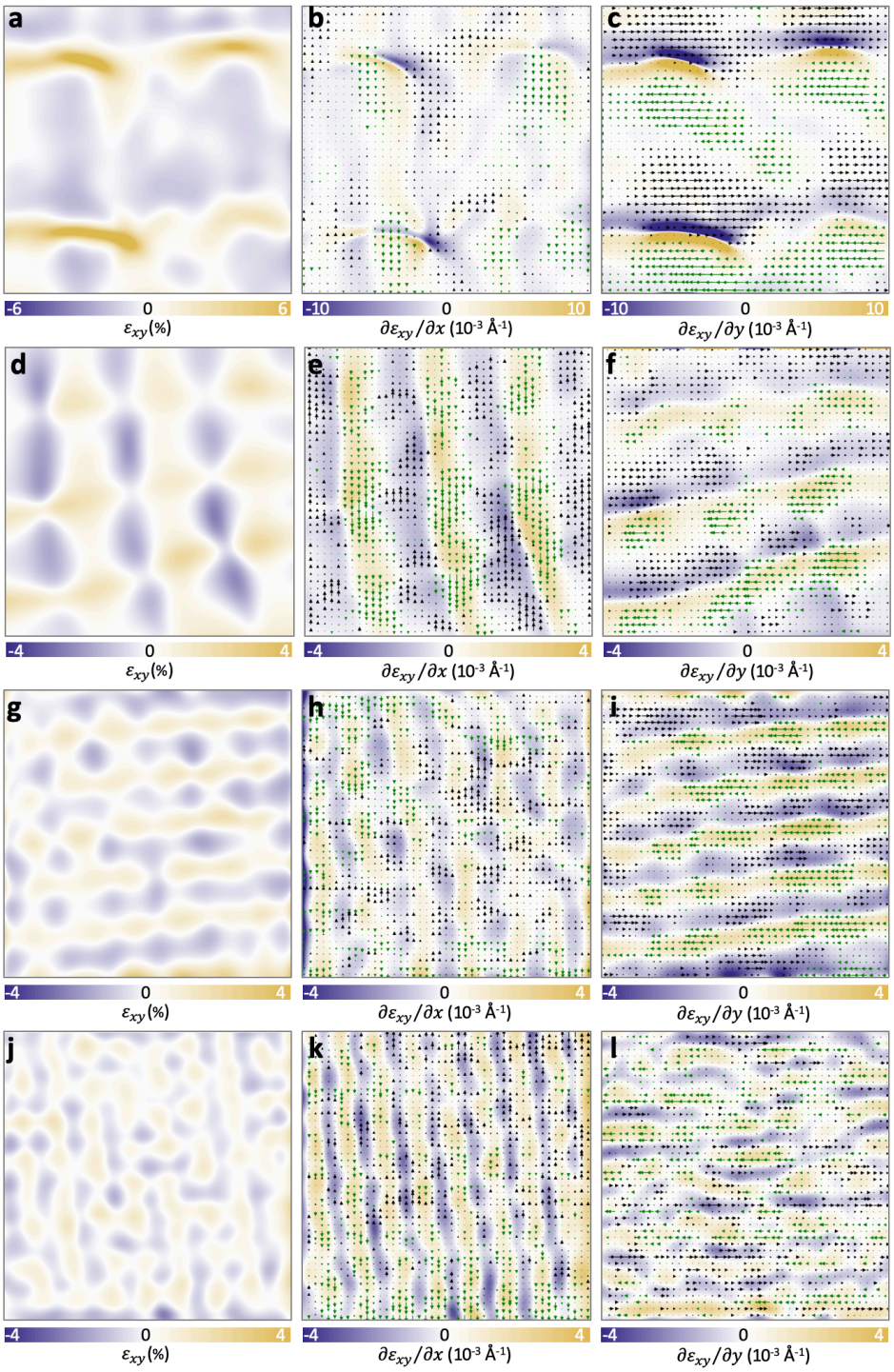

Supplementary Figure. S10. a, Shear strain (ε_{xy}) component map for the top layer in 3.0° twisted bilayer. **b-c**, Corresponding shear strain gradient maps along the *x*-axis and *y*-axis, respectively, superimposed with Ru displacement components along the *y*-axis and *x*-axis. The strain gradients ($\varepsilon_{xy,x}$ and $\varepsilon_{xy,y}$) can generate flexoelectric field components in the *y*-direction and *x*-direction, respectively. Same shear strain (gradients) analyses for **d-f**, the 4.8° twisted, **g-i**, the 7.4° twisted and **j-l**, the 10.4° twisted bilayers. The Ru displacement components in **b-c**, **e-f**, **g-i**, and **j-l** are amplified by a factor of 30, 50, 100, and 120 for clarity, respectively.

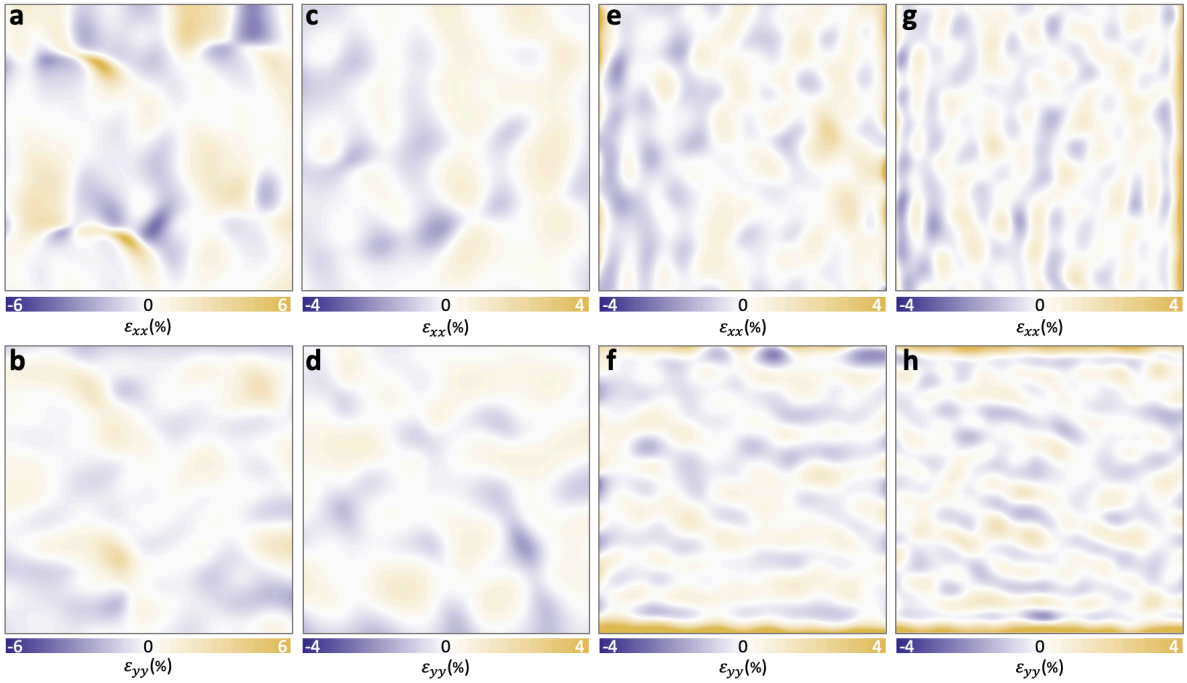

Supplementary Figure S11. a, Normal strain (ε_{xx}) along the *x*-axis and **b**, normal strain (ε_{yy}) along the *y*-axis of the top layer in the 3.0° twisted bilayer. Same strain analyses for **c**-**d**, the 4.8° twisted, **e**-**f**, the 7.3° twisted, and **g**-**h**, the 10.4° twisted bilayers.

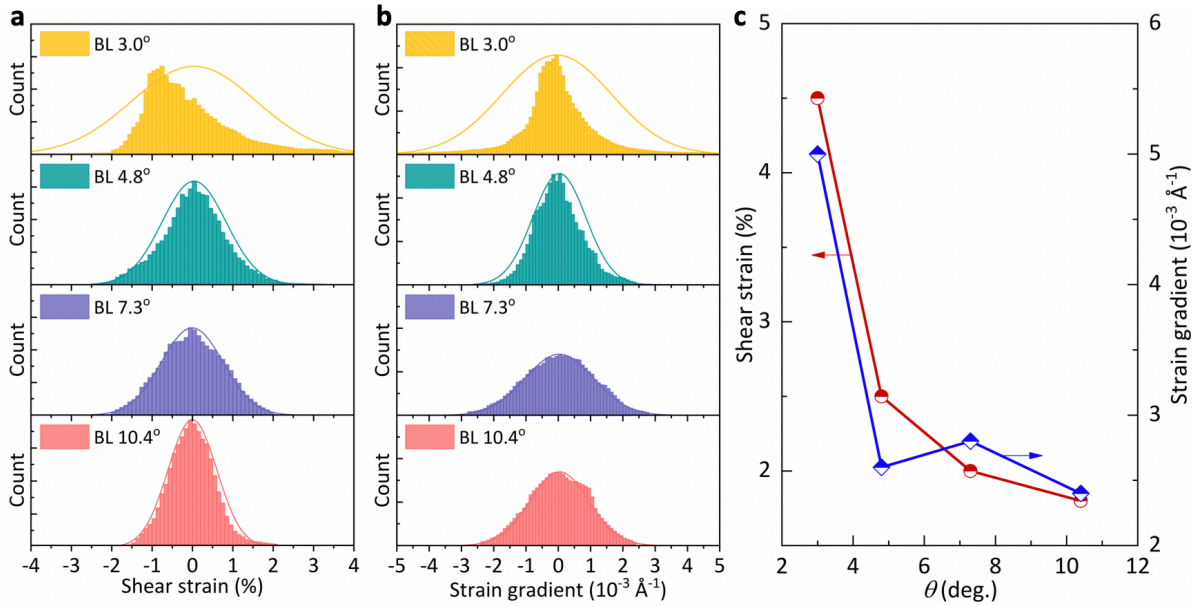

Supplementary Figure S12. Histograms comparing **a**, the shear strains and **b**, shear strain gradients of t-BL SROs. **c**, Twist angle dependence of the maximum absolute strain and strain gradient.

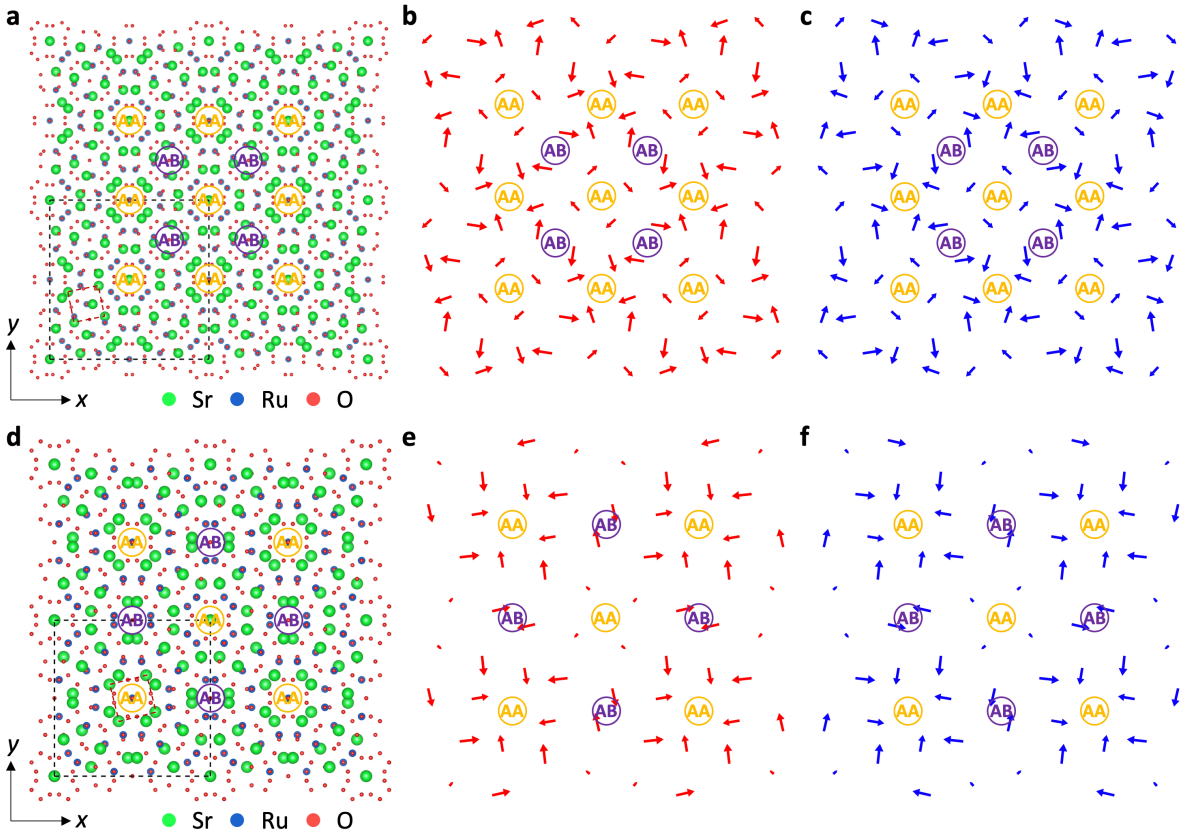

Supplementary Figure S13. **a**, Planar-view of constructed 2x2 supercell for the 22.62° twisted bilayer. The black and red dashed squares denote the supercell and unit cell, respectively. **b-c**, In-plane Ru displacement maps of the top and bottom SRO layers, respectively. **d-f**, Same analyses for the 28.07° twisted bilayer. All displacements are amplified by a factor of 25 for clarity. The AA- and AB-stacked regions are marked with yellow and purple circles, respectively.

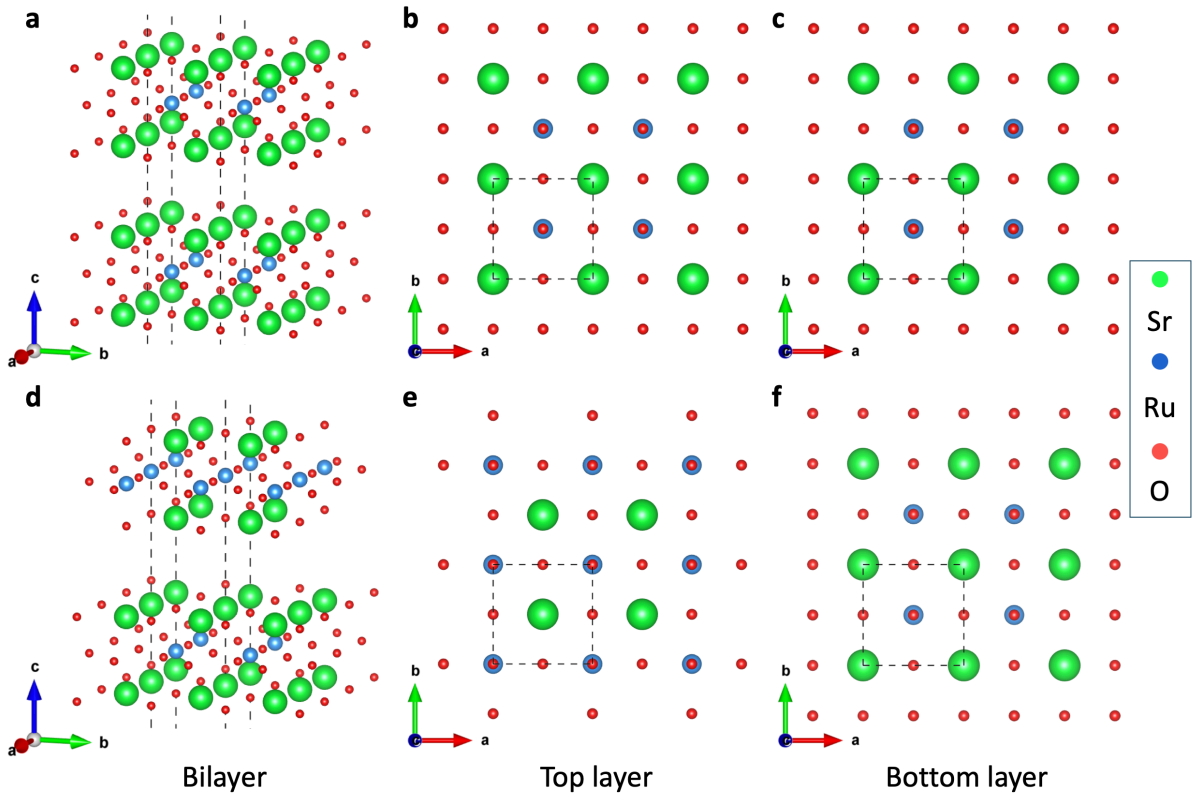

Supplementary Figure S14. a, 3D-view of the constructed 2x2 supercell structure for the 0°-stacked bilayer with AA-stacking. **b-c**, Planar-view of the relaxed lattice of the top layer and bottom layer, respectively. **d-f**, Same calculations for 0°-stacked bilayer with AB-stacking. Irrespective of AA- or AB-stacked configurations, the SRO maintains a centrosymmetric structure without any Ru displacement.

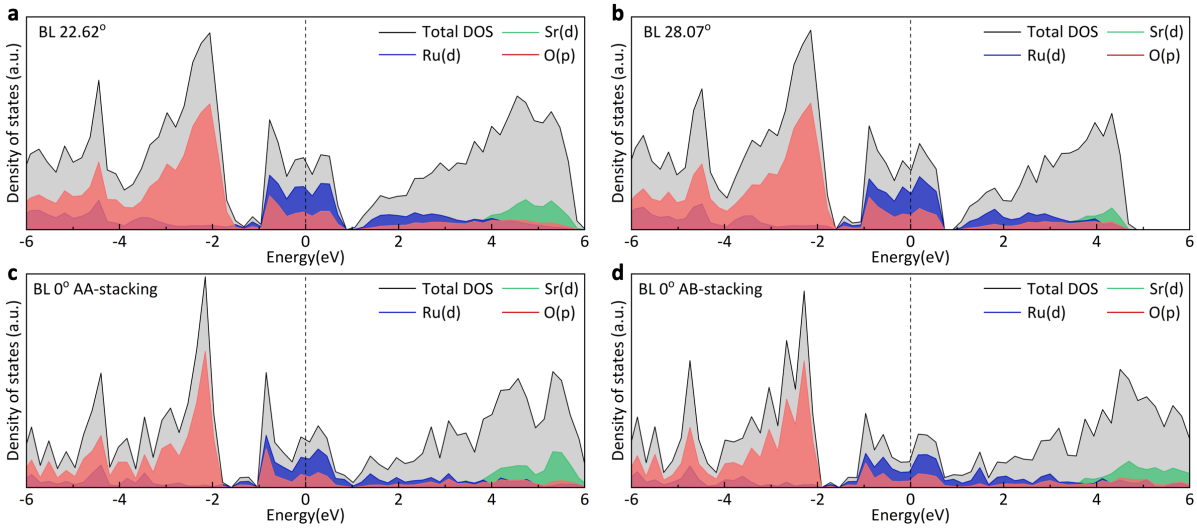

Supplementary Figure S15. Electronic density of states (DOS) of **a**, the polarized 22.62° twisted bilayer. **b-d**, Same calculations for the polarized 28.07° twisted bilayer, and the unpolarized 0°-stacked bilayer with AA- and AB-stackings, respectively. All results show nonzero density of states at the Fermi level, primarily contributed by the *d*-orbital electrons of Ru atoms, suggesting that SRO retains its metallic nature in both twisted and un-twisted bilayers.

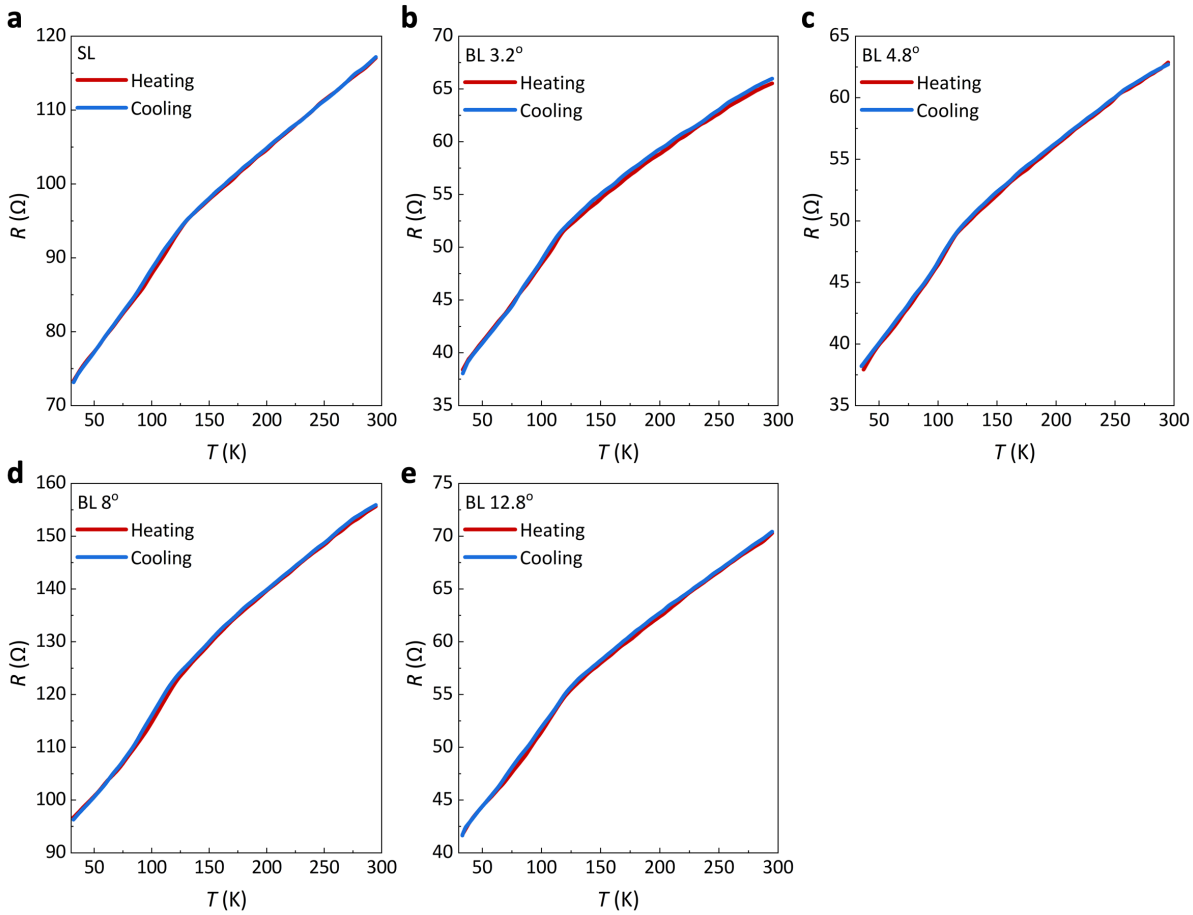

166

167 **Supplementary Figure S16.** Temperature-dependent resistance curves of SL and BL SROs with
168 twist angles ranging from 3.2° to 12.8°. The measurements were conducted separately in
169 heating and cooling modes under a temperature range of 35 - 295 K. The heating and cooling
170 curves coincide with each other. Accurately comparing the resistance among t-BL SROs is
171 challenging due to the difficulty in precisely determining the conductive area, which is affected
172 by unavoidable microcracks.

173

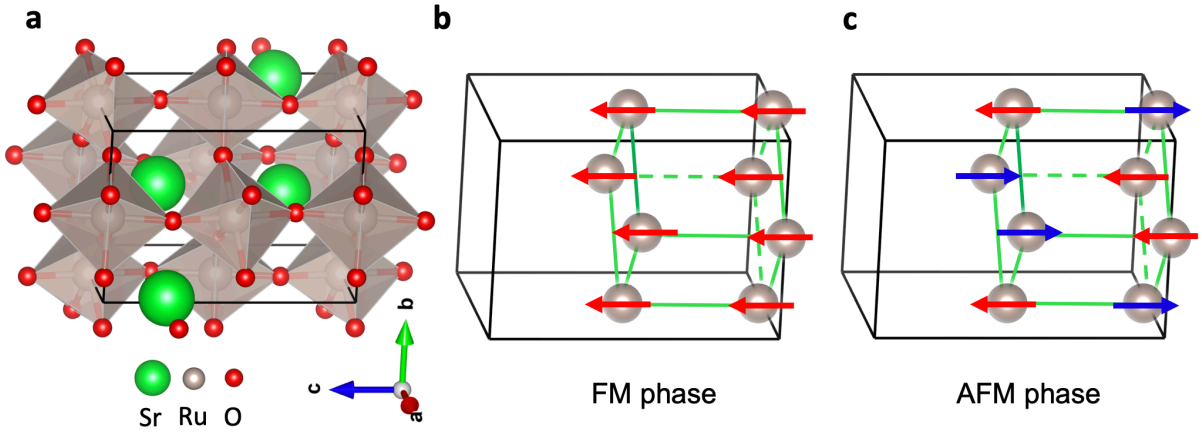

Supplementary Figure S17. a, Orthorhombic structure of $SrRuO_3$ used in DFT magnetic calculation. Spin configurations of **b,** ferromagnetic (FM) and **c,** G-type antiferromagnetic (AFM) phase.

References

1. Hÿtch, M. J., Snoeck, E. & Kilaas, R. Quantitative measurement of displacement and strain fields from HREM micrographs. *Ultramicroscopy* **74**, 131–146 (1998).
2. Ma, W. A study of flexoelectric coupling associated internal electric field and stress in thin film ferroelectrics. *Phys. Stat. Sol. (b)* **245**, 761–768 (2008).
3. Seto, Y. & Ohtsuka, M. ReciPro: free and open-source multipurpose crystallographic software integrating a crystal model database and viewer, diffraction and microscopy simulators, and diffraction data analysis tools. *J. Appl. Crystallogr.* **55**, 397–410 (2022).